Large Eddy Simulation of laser ignition and compressible reacting flow in a rocket-like configuration

Guilhem Lacaze, Bénédicte Cuenot, Thierry Poinsot, Michael Oschwald

Large Eddy Simulation of laser ignition and compressible reacting flow in a rocket-like configuration

G. Lacaze [a], B. Cuenot [a], T. Poinsot [b] and M. Oschwald [c]

[a] *CERFACS, 42 Avenue G. Coriolis, 31057 Toulouse cedex, France*

[b] *Institut de Mécanique des Fluides de Toulouse, CNRS, Avenue C. Soula, 31400 Toulouse, France*

[c] *DLR Lampoldshausen, 74239 Hardthausen, Germany*

Abstract

The control of ignition in a rocket engine is a critical problem for combustion chamber design. Delayed ignition may lead to high amplitude pressure fluctuations that can damage the burner (strong ignition) whereas early ignition may fail. This paper describes a numerical study of a strong ignition sequence observed in a laboratory-scale single-injector rocket chamber ignited by a laser and fueled with gaseous oxygen and hydrogen. OH-emission images, Schlieren pictures and pressure measurements allow to follow the flame propagation experimentally. The present Large Eddy Simulation (LES) approach includes shock treatment, a 6 species - 7 reaction chemical scheme for $H_2 - O_2$ and a model for the energy deposition by a laser. Flame/turbulence interaction is modeled with the thickened flame concept. LES is used to compute both the filling phase (during which the gaseous hydrogen and oxygen mix) and the ignition phase. The flame location and structure as well as the temporal evolution of the chamber pressure obtained numerically are in good

agreement with the experiment. The use of complex chemistry in the computation also allows the comparison of LES data with experimental OH-images and shows that the sensitivity of the CCD camera used to record the spontaneous emission of the $OH*$ radical is not high enough to properly locate the flame front in rich regions. The combined experimental and numerical results lead to a more detailed analysis of the ignition processes and its coupling with flow rates oscillations in the H_2 and O_2 feeding lines.

Key words: IGNITION, NUMERICAL COMBUSTION, ROCKET ENGINES

1 Introduction

Understanding ignition processes is extremely important to design reliable combustion devices. The technical needs for internal-combustion (IC) engines and aircraft combustors have motivated a large range of theoretical, experimental and numerical studies on ignition phenomena. Under uniform mixture condition with no flow, the minimum energy to trigger a chemical run-away as well as the critical radius and the duration of the spark have been extensively studied, analytically and experimentally [1–4]. In turbulent premixed flows, stretch and convective effects can lead to the failure of ignition [2,5–7]. In turbulent non-premixed configurations such as jet and bluff-body flows, ignition failure is mainly due to incomplete mixing at the spark location [8,9]. Other studies of Ballal and Lefevre [10] and of Danis [11] show the influence of two-phase flow effects on spark ignition.

In rocket engines ignition is a critical phase for safety and payload-cost constraints. The development program of future launchers often focusses on multiple-payload capability based on re-ignitable upper stage engines. In this context,

ignition control is critical as it must be repeatable without failure.

The combustion initiation in rocket engines is usually based on pyrotechnic devices. Burned gases are injected into the chamber while the valves of propellants are simultaneously opened. Ignition in such configurations is mainly driven by turbulent mixing, convective effects, thermodynamic conditions, interaction between the under-expanded pyrotechnic jet and propellants jets, chemistry and two phase flow effects [1]. Most of these processes have been studied separately but due to measurement difficulties, experimental data on rocket ignition transient is limited [12–17]. McManus et al. [12] have investigate ignition processes recording the laser-induced fluorescence of the OH radical in a combustion chamber composed of three injectors fed with gaseous hydrogen and air. Ignition was triggered by a spark plug and the experiment showed that after the initiation of the kernel, the flame propagated in a partially premixed mode before stabilizing in a diffusion mode. Mayer et al. [13] studied the atomization of a liquid oxygen jet by a surrounding gaseous hydrogen jet and the effect of ignition on atomization processes. Gurliat et al. [16] and Schmidt et al. [15] have experimentally studied laser ignition sequences of a gaseous hydrogen and liquid oxygen ($GH_2 - Lox$) spray in a small scale combustion chamber with a single shear coaxial injector. Smooth and strong ignition processes were analyzed via high speed OH-imaging and Schlieren images. De Rosa et al. [17] reproduced the analysis of [16] under vacuum conditions.

Numerical simulations of rocket ignition are mainly based on the Reynolds Averaged Navier-Stokes (RANS) approach : for example, Schmidt et al. [14] and Karl et al. [18] carried out simulations of the ignition sequence of the laboratory-scale rocket engine operated at the Lampoldshausen DLR center [19]. The numerical study presented in [14] did include out the entire

ignition sequence. In [18] the DLR-Tau code was used and results showed how the flame propagated in the whole chamber volume but overpredicted the maximum value of the pressure by 45% compared to experiment. The authors explained this result by the fact that the calculation was performed in two dimensions without nitrogen dilution (the filling phase was not simulated) and without turbulence effects.

Large Eddy Simulation (LES) is a powerful tool to study unsteady complex flows. The concept of explicitely solving for the large geometry-dependent turbulent scales while modelling the dissipative behavior of the smaller scales, combined with high order numerical schemes and optimized unstructured meshes, has already shown its accuracy for turbulent non-reacting [20–22] and reacting flows [23–25] and recent results obtained on burners of gas turbine configurations have revolutionized the field of CFD combustion [26–30]. The application of LES to unsteady combustion in rocket engines is more recent [31–33] and more complex due to the particular thermodynamics and flow-dynamics conditions.

The first objective of this paper is to present a LES methodology applied to the problem of ignition in rocket engines. The compressible nature of the flow (with sonic inlets and shocks), the fast $H_2 - O_2$ chemistry and high pressure effects require specific developments that are presented here. The second aim of this study is to validate numerical results against the experiment of DLR [19], to establish an ignition scenario and to identify the important physical phenomena on the basis of a complementary analysis of numerical and experimental data.

The paper is organised as follows : section 2 describes the phenomenology and physics of ignition in rocket engines and section 3 presents the ignition experiment. Section 4 develops the LES methodology and the numerical approach

required to apply LES to compressible reacting flows. The computational configuration is described in section 5 and results are analysed in section 6.

2 Ignition of liquid rocket engines

Ignition of liquid rocket engines is characterized by high-speed injection jets and very fast chemistry, making the ignition time a key-parameter for the success or failure of ignition : if it is too short, reactants are not sufficiently mixed to react strongly enough compared to the short convective time and to sustain combustion. If it is too long, the mixed reactants ignite too strongly and generate high and dangerous pressure levels [34–36].

Figure 1 shows a simplified sketch of an injection plate of a cryogenic rocket engine supporting hundreds of coaxial injectors feeding a chamber connected to the exit nozzle. The ignition of such an engine follows a specific sequence controlled by the timing of the valves opening. A usual ignition sequence may be described in four phases : first the system is purged with an inert gas (Helium) to reach a nominal state and to cool down injection lines. Then the fuel injection (usually hydrogen) starts and after a few milliseconds the igniter is triggered. In real engines, the igniter is either a pyrotechnic system or a spark torch usually located at the center of the injection plate (producing a strongly under-expanded jet in the chamber) that blows a stream of hot gases. Finally the oxidizer (oxygen) valve is open, and the oxygen injected into a hot flow containing fuel allows combustion to start [34–36]. In the present experiment, the ignition sequence is slightly different as described in the next section to allow a better control and a more precise analysis of the ignition events.

3 The M3 burner experiment

The M3 burner experiment operated at DLR [19] has been designed to investigate primary ignition processes and combustion in a rocket-like configuration using optical diagnostics [15–17]. Propellants may be either cooled by liquid nitrogen for cryogenic tests or injected under ambient conditions. A parameter study was performed to evaluate the impact of injection conditions on ignition at ambient pressure and temperature. In the experiment, ignition is triggered with a Nd:YAG ($\lambda = 532\ nm$) laser. All injection regimes presented in [19] correspond to delayed ignition, with a long intake phase that fills the chamber with a $H_2 - O_2$ gaseous mixture before laser ignition. In real rocket engines, an accidental delay in ignition may lead to a similar situation. Indeed, an ignition delay leads to the evaporation of an important amount of liquid oxygen and thus to the creation of a significant volume of gaseous flammable mixture into the chamber as in the present experiment. After ignition the flame spreads over the whole chamber leading to a sharp pressure peak. Once the mixture is burned, a diffusion flame anchors at the injector lips [19].

The test rig is fueled with gaseous hydrogen and oxygen by a coaxial injector and connected to the atmosphere by an exhaust nozzle (Fig. 2). The chamber is a 14 cm long box with a square section (6x6 cm^2) designed to sustain pressures up to 20 bars. Complete optical access to the chamber volume is obtained via two opposed quartz windows. Smaller windows are placed on the two other sides to introduce the igniting laser beam. Burned gases exhaust through a 4 mm diameter nozzle which chokes during the ignition sequence. The coaxial injector is a 1.22 mm diameter O_2 injection tube surrounded by a

H_2 injection annulus with an inner diameter of 2 mm and an outer diameter of 4 mm (Fig. 2).

To study of the ignition phase (that only lasts about 5 ms), experimental diagnostics have to be accurately synchronized with the ignition time. With a standard pyrotechnic igniter, the position and the chemical run-away time vary drastically from one test to another. Previous tests, using a pilot flame to initiate combustion in the M3 burner, have shown that this method was not suitable for the present study [13]. Laser was chosen to initiate combustion and was found to give repeatable ignition times [14,16,19]. A second advantage of laser ignition is to allow an accurate location of the energy deposition without disturbing the flow contrary to electrical spark systems. In the experiment the laser ignites the mixture by an energy deposition of 195 mJ over 10 ns per pulse [19]. The beam is focused in the mixing layer between the reactant jets, at 36 mm downstream of the injection plate and at 2.5 mm above the injector axis (Fig. 2b). Schlieren images show that a hot plasma develops within an ellipsoid of 3.5 mm diameter and 2 mm length in the axial direction. No change of the global flame behavior was reported for energy depositions varying between 80 and 195 mJ [19].

The spontaneous OH-emission of the flame is captured by an intensified CCD-camera (Photron Fastcam Ultima I^2) with an interference filter that only transmits radiations emitted by OH radical (300-310 nm). The 256x64 pixel pictures are recorded at a rate of 18kHz. The flow topology and the flame development are visualized via Schlieren photographs, recorded with a Hasselblad film camera at a frame rate of 4kHz and an aperture time of 13 μs [19].

Schlieren images show density gradient fields (detecting the variation of refractive index into the gas) i. e. location of species segregation and transition from fresh to hot-burned gases. In addition to the optical set-up, pressure and temperature sensors are placed in the hydrogen and oxygen injection domes (Fig. 2b) while static pressure is also measured in the chamber. The chamber pressure sensor is located 44 mm downstream of the injection plate in the middle of the top wall. Temperatures and pressures are recorded at a rate of 4.35 kHz [19].

The experiment is operated at room temperature ($\approx$ 300 K) and pressure ($\approx$ 1.013 bar). Mass fluxes of hydrogen and oxygen are estimated thanks to choked nozzles located upstream of the domes in the injection lines (Table 1). In order to define a reference condition, the chamber and the injection lines are purged with N2 before each test (Table 2). Once nitrogen injection is stopped the injection of propellants starts. Hydrogen and oxygen are injected at a mixture ratio of $\dot{m}_{O_2}/\dot{m}_{H_2} = 2$ corresponding to an equivalence ratio of 4. During this injection phase, H_2 is first injected alone for 7 ms, before the O_2 valve is opened. The injection phase then lasts 370 ms before the laser is triggered.

4 LES methodology

The computation of the laser ignition sequence of the M3 burner requires particular numerical developments to correctly reproduce the different phases of the transient process : a compressible LES solver (section 4.1), a method to handle shocks (section 4.2), a model for laser ignition (section 4.3) and a

$H_2 - O_2$ chemical scheme (section 4.4).

4.1 Explicit compressible LES solver

A fully unstructured solver is used to advance the compressible Navier Stokes equations for a multi-species gas using perfect gas laws [37]. For these ignition conditions, pressure is low and there is no need to include real gas effects [31]. Realistic thermochemistry is used, allowing multi-step kinetics for the oxidation of hydrogen [38]. The Lax-Wendroff scheme [39] (centered differencing) with a second-order accuracy in space and time and explicit time-advancement are used to control numerical dissipation and capture acoustics. The time step is controlled by the CFL number based on the sum of the convective and sound speeds. Sub-grid scale turbulent viscosity ν_t is calculated with the Smagorinsky model [40]. Turbulent diffusivities for energy and species are obtained from ν_t using respectively $D^t_{th} = \nu_t / Pr_t$ and $D^t_k = \nu_t / Sc_t$, where Pr_t is the turbulent Prandtl number (equal to 0.6) and Sc_t is the turbulent Schmidt number (equal to 0.6 for all species). Characteristic boundary conditions are set with the NSCBC method [41,37].

A summary of the LES equations solved by the code is given below [24] :

$$\frac{\partial \overline{\mathbf{w}}}{\partial t} + \nabla \cdot \overline{\mathbf{F}} \; = \; \overline{\mathbf{S}}_{\mathbf{c}} \tag{1}$$

where $\overline{\mathbf{w}}$ is the vector of transported variables, $\overline{\mathbf{F}}$ is the flux tensor composed of viscous, inviscid and subgrid scale components and $\overline{\mathbf{S}}_{\mathbf{c}}$ is the chemical source term. $\overline{\mathbf{w}}$ and $\overline{\mathbf{S}}_{\mathbf{c}}$ are given respectively by :

$$\mathbf{w} = (\rho u, \rho v, \rho w, \rho E, \rho_k)^T \;\; \text{and} \;\; \overline{\mathbf{S}}_{\mathbf{c}} = (0, 0, 0, \dot{\omega_T} + \dot{Q}, \dot{\omega_k})^T \tag{2}$$

where ρ is the density, $\mathbf{u} = (u, v, w)^T$ the velocity vector, the total energy per unit mass is defined by $E = \frac{1}{2}\mathbf{u} \cdot \mathbf{u} + E_i$ where E_i is the internal energy and $\rho_k = \rho Y_k$ where Y_k is the mass fraction of species k. The models for the reaction rates $\dot{\omega_k}$ and the heat release $\dot{\omega_T}$ (Eq. 2) are described in section 4.4. The $\dot{Q}$ term is the power deposited by the laser (section 4.3).

To handle flame/turbulence interaction, the dynamically thickened flame model (TFLES) is used [29,30,42,43]. This model thickens the flame front so that it is resolved on the LES grid (usually on 5 to 8 points). The turbulent sub-grid scale wrinkling of the flame is modeled through the so-called efficiency function (based on the local sub-grid scale turbulence velocity and length scale), E [44] which allows to recover the turbulent flame speed. The TFLES model has been applied successfully to several configurations (premixed and partially premixed) and more details can be found in [27,29,42,44,45].

4.2 Shock treatment

The conditions of injection in rocket engines lead to supersonic under-expanded jets with shocks in a succession of expansion/recompression cells [46]. In the M3 burner, just before ignition, the oxygen dome is at 12 bar whereas the chamber is at about 2 bar. This pressure difference results in a supersonic jet with a tiger-tail-like shape. Because the LES code uses centered differencing the positivity of the solution in near shock region is not maintained due to strong gradients. To capture shocks, the methodology of Cook and Cabot [47] is used. It thickens the shock front by introducing a hyper-viscosity β (which

can be seen as a bulk viscosity) in the viscous stress tensor $\underline{\tau}$:

$$\underline{\tau}_{modified} = (\beta - \frac{2}{3}\mu)\ \nabla.\mathbf{u}\ \underline{\delta} + 2\mu\underline{S} \tag{3}$$

where μ is the dynamic viscosity and $\underline{S}$ is the symmetric strain rate tensor. The bulk β viscosity is modeled as :

$$\beta = C(\Delta x)^4 |\nabla^2 \underline{S}| \tag{4}$$

where C is fixed to 5 according to [47]. This hyper-viscosity acts on the very sharp velocity gradients characterizing shocks but goes to zero where the velocity evolves smoothly. Tests have shown that it has a minor effect on the LES quality away from shocks and flames. This hyper-viscosity term is equivalent to an additional pressure term (P_{Cook}) :

$$P_{Cook} = -\beta \frac{\partial u_k}{\partial x_k} \tag{5}$$

This approach was validated on simple one-dimensional shock-tube cases and on other more complex configurations. Figure 3 presents velocity profiles for a shock tube problem, given by the theory [48] and by numerical simulation with and without bulk viscosity. The approach of Cook suppresses spurious values of the velocity in the shock region. This approach was also successfully tested by Fiorina and Lele [49] on various 2D configurations such as oblique shock waves, a supersonic blunt body flow and a Mach reflection problem.

4.3 Laser model for ignition in LES

Multiple models have been proposed to describe ignition in premixed conditions [50–53]. For the present case, ignition takes place in a non-premixed flow

and a model (called ED for Energy Deposition in the rest of the text) was used to describe the ignition phase. The main idea of the ED model is to represent ignition by a source term directly added to the energy equation. This method was already used in several numerical works (Direct Numerical Simulations) to study the early times of flame generation in quiescent homogeneous mixtures [54,55] and in turbulent inhomogeneous flows [56]. It is applied here in the LES context.

In the present computation, the model represents the effect of the spark after the time when the kernel temperature has decreased below the ionization temperature (Fig. 4) and gas ionization is not taken into account. In the ED model, the energy injected in the calculation is the energy transferred from the plasma to the gaseous mixture. For laser ignition this energy accounts for about 10% of the laser energy [57,58] (most of the initial energy is lost in the induced shock wave).

The laser energy is represented by a power $\dot{Q}$ added to the energy equation (Eq. 2). The $\dot{Q}$ term is a gaussian distribution in time and space deposited at the beam focus location :

$$\dot{Q}(x,y,z,t) = \frac{\varepsilon_i}{4\pi^2\sigma_r^3\sigma_t} e^{-\frac{1}{2}(\frac{r}{\sigma_r})^2} e^{-\frac{1}{2}(\frac{t-t_o}{\sigma_t})^2} \tag{6}$$

where r is the distance to the laser focus center, t_o is the time when $\dot{Q}$ is maximum, ε_i is the total amount of deposited energy and σ_r and σ_t are the spatial and temporal widths of the deposition.

The ED model has been validated in a laminar premixed case (Erard et al. [59]), where a propane-air mixture at ϕ=1 and 1 bar is ignited with an electrical spark. Results from the three-dimensional simulation agree with ex-

perimental measurements as presented on Fig. 5, showing that the assumptions of the ED model are reasonable.

For the present study, the energy deposition is focused at the same location as in the experiment. Additional numerical resolution near the laser point is required to compute the initial kernel formation. In the LES the grid size at laser focus point is 0.1 mm which is approximately the thickness of the flame in the conditions (mixture and thermodynamics) of this region. The total amount of energy transferred to the mixture is set to 40 mJ (i.e. 20% of the laser energy) in a 3mm-radius sphere during 0.5 μs.

4.4 Chemical kinetics

A seven-step chemical scheme (called H2O2-GL7-1 in the rest of the paper) using six species (H_2, O_2, H_2O, OH, O, H) extracted from the work of Baurle et al. [38] is used (Tab. 3). It has been modified to accurately reproduce the laminar flame speed and adiabatic temperature over a large range of equivalence ratio and to take into account pressure effects. Indeed, the chamber pressure initially equal to 1.85 bar reaches 11 bar during the ignition sequence and the effect on chemistry is significant. Figure 6 shows the comparison between detailed chemistry [60] and the seven-step scheme for the prediction of the flame speed at different equivalence ratios and at 1 bar. The laminar flame velocity is predicted with a maximum error of about 10% around an equivalence ratio of 1.5 and is correct for both lean and rich conditions. Pressure effects are more difficult to assess quantitatively as there are no measurements and detailed chemistry calculations do not agree, as shown in fig. 7 where three detailed

chemical schemes from O'Conaire et al. [60], Kee et al. [61] and Smooke et al. [62] are compared with the reduced H2O2-GL7-1 scheme. The velocity obtained with the reduced scheme is in the range of the three complex schemes. For the present simulation, ignition delay is also a key parameter : the laser beam induces a local temperature rise that triggers the chemical run-away by auto-ignition. An example of the performance of the 7-step scheme is given on Fig. 8 where it is compared to the detailed scheme of O'Conaire et al. [60]. Results for both schemes are of the order of the micro-second at temperatures around 2000 K. The differences observed on Fig. 8 have thus no significant impact on the kernel flame creation which characteristic time is in the order of 100 μs [19]. When energy is deposited in a H_2/O_2 mixture with the ED model, the temperature rises locally up to several thousands of Kelvins and few time after the initiation reaction ($H_2 + O_2 \leftrightarrow OH + OH$) starts almost immediately as shown on Fig. 9 on a one-dimensional case. This reaction creates the first OH radicals that will trigger the chain-branching reactions. Figure 9 presents an induction time after the reaction peak of the initiation reaction. During this time, all reactions start and their respective reaction rates increase exponentially until around $t = 8\ \mu s$ which is the run-away time. At this time the flame kernel is created and starts to propagate as a spherical flame.

4.5 Boundary conditions

Boundary conditions are treated with an approach based on the method of characteristics [37,41]. The hydrogen inlet remains subsonic during the whole experiment : its mass flow rate and static temperature (Tab. 1) are imposed at the H_2 dome inlet (Fig. 10b). The exit boundary (which is located outside the

chamber, Fig. 10b) is relaxed to the ambient pressure. The walls in the injection lines and in the exhaust nozzle are adiabatic slip walls, while the chamber walls integrate heat losses (for brevity this aspect has not been developed in this paper, more details are available in [63]).

In this configuration the oxygen inlet velocity is first sonic and then subsonic when the chamber pressure increases. The moment when the flow becomes subsonic is obtained by the calculation of the Mach number M at the injection section. M is calculated with isentropic nozzle relations applied between the injection dome (total pressure : P_i) and the chamber (total pressure : P_c).

In sonic conditions, the momentum is defined by [64] :

$$\rho u_{inj} = \frac{P_i}{(r.T_i)^{1/2}} \gamma^{1/2} \left(\frac{2}{\gamma+1} \right)^{\frac{\gamma+1}{2(\gamma-1)}} \tag{7}$$

where T_i is the total temperature in the dome, $\gamma = C_p/C_v$ is the ratio of the heat capacities and $r = R/W_{mel}$ where R is the universal gas constant and W_{mel} the molar mass of the injected mixture. The static temperature and pressure at injection are deduced from isentropic relations :

$$T_{inj} = \frac{2}{\gamma+1} T_i \quad \text{and} \quad P_{inj} = \left(\frac{2}{\gamma+1} \right)^{\frac{\gamma}{\gamma-1}} P_i \tag{8}$$

In subsonic conditions, only the mass flux and temperature are imposed. They are calculated from the isentropic relations now involving the chamber pressure P_c :

$$\rho u_{inj} = \frac{P_i}{(rT_i)^{1/2}} \left(\frac{P_c}{P_i} \right)^{\frac{1}{\gamma}} \left(\frac{2\gamma}{\gamma-1} \left(1 - \left(\frac{P_c}{P_i} \right)^{\frac{\gamma-1}{\gamma}} \right) \right)^{1/2} \tag{9}$$

$$T_{inj} = \left(1 + \frac{\gamma-1}{2} M^2 \right)^{-1} T_i \tag{10}$$

If $M = u_{inj}/(\gamma r T_{inj})^{1/2} \geq 1$, where u_{inj} is the predicted (calculated) inlet velocity, Eqs 7 and 8 are used, otherwise, Eqs 9 and 10 are used to determine inlet conditions. The mass flux is $\dot{m} = AC_d\rho u_{inj}$, where A is the throat section of the injector (Fig. 10b) and the discharge coefficient C_d is kept constant for the whole calculation and is estimated to 0.346.

Figure 11 presents the temporal evolution of the oxygen injection mass flux during the calculation and compared to the experiment showing that the injection history is well represented by the present approach. Variations of the injection flux observed in the subsonic regime are due to the presence of a longitudinal pressure fluctuation.

5 Numerical configuration

The numerical configuration reproduces the 3D combustion chamber with the H_2 dome, the O_2 inlet tube, the exit throat and the atmosphere (Fig. 10). The H_2 dome is included in the computational domain to capture the back-flow into the hydrogen injection line observed in the experiment [19]. This back-flow is due to the fact that the chamber pressure becomes higher than the H_2-dome pressure during a portion of the ignition sequence. To minimize the impact of the exit boundary condition, the atmosphere around the chamber outlet is also calculated. The mesh is refined around the jets at inlet and downwards where they mix, develop and are ignited by the laser beam. It is fully unstructured and uses tetrahedral cells (Fig. 10c). It contains 645,000 nodes and 3,500,000 cells, with the smallest and biggest cell characteristic size being of the order of 0.2 mm and 2 mm respectively.

5.1 Initial conditions

The computation of the ignition sequence is performed in two steps. In the filling phase the chamber initially full of nitrogen at 300 K and at a pressure of 1.013 bar, is purged with gaseous O_2 and H_2. Then in the second phase the ignition and the propagation of the flame are computed. Most of the filling phase (from 0 to 368 ms) is computed on a coarse mesh (390,000 nodes) and only the last instants (from 368 to 370 ms) are computed on the fine mesh (Fig. 10c), to increase the jet topology accuracy before the energy deposition.

6 Results and discussions

6.1 Cold flow and mixing

The flow field is first studied after 370 ms of the filling phase, i. e. just before laser ignition. At this instant, the chamber pressure and temperature are respectively equal to 1.75 bar (1.87 bar in the experiment) and 350 K. The instantaneous axial velocity field obtained by LES shows the turbulent jet and the large recirculation zones (visualized with the 0-velocity isoline on Fig. 12). The oxygen jet is underexpanded and is injected at 350 m/s and reaches a maximum velocity of 650 m/s (Mach 1.9) while the maximum velocity in the hydrogen jet is 470 m/s. Figure 13a) shows a field of the Z-component of the vorticity in the jet region and the instantaneous velocities along the axis of the O_2 and H_2 jets are presented on Fig. 13b). The hydrogen jet decays rapidly after about 5 mm and its production of vorticity stops after 15 mm, however, as the oxygen jet expands, it keeps a coherent structure until 25 mm

downstream of the injection plate. After 25 mm both jets interact, enhancing mixing and turbulence production : at the laser focus point, axial velocity fluctuations represent about 20% of the mean axial velocity. The sonic O_2 jet leads to the formation of expansion/compression cells that are progressively damped by the flow. Figure 14 is a comparison at ignition time of a Schlieren image and the numerical pressure field showing a good qualitative agreement in the jet pattern. In particular the size of the cells is reproduced.

The time evolution of the mass fraction of nitrogen during the filling phase is presented on Fig. 15 showing that some nitrogen remains in the chamber at the ignition time with a maximum value of 0.17 and a mean value of 0.14. Most of the nitrogen is trapped in the recirculation zones in the corners of the chamber. This amount of residual nitrogen will have an impact on the pressure peak value after ignition. Indeed two 0D equilibrium calculations at constant volume have been carried out with a $H_2 - O_2$ mixture (at the overall equivalence ratio of the 3D simulation which is 4) and with and without the N_2 dilution of 14% in mass. The calculation without nitrogen gives final temperature and pressure of respectively 2735 K and 15.0 bar while with N_2 dilution, 2486 K and 13.8 bar were obtained, which represents a 10% difference on the final temperature and 9% on the pressure. The reactants are well mixed in most of the chamber as shown on Fig. 16 where the field of the equivalence ratio is displayed as well as the line ϕ =3. Mixture gradients are only present in the jet region whereas in the recirculation zone, the equivalence ratio is close to ϕ =4 which is the overall injection equivalence ratio.

6.2 Ignition and combustion

The main experimental result is the pressure time evolution after ignition shown on Fig. 17. LES (also plotted on Fig 17), shows a good agreement with measurements. The value of the pressure peak in the LES (11.2 bar) is close to the experiment record (11.1 bar), but appears slightly earlier (about 0.25 ms) resulting in a shift between the two curves in the decreasing phase. This shows that the mixture obtained in the chamber after the intake phase is close to the experimental conditions and that the consumption rate is correctly predicted.

Flame propagation can be estimated experimentally from Schlieren photographs. LES results can also be used to reconstruct pseudo-Schlieren pictures from the calculation of density gradients integrated across the chamber. Experimental and numerical Schlieren images at three different times after ignition (Fig. 18) show the positions of the flame front (in the present case, as the chamber is initially full of partially mixed reactants, the Schlieren pictures that locate the limit between hot and cold gases also indicate the position of the flame surface). The topology of the flame at the three times (35 μs, 250 μs and 680 μs) is well captured by LES.

The spontaneous emission of the OH radical visualized experimentally can be compared to the reaction rate calculated in the LES [7]. For this comparison, the reaction rate of the reaction: $H_2O + O \leftrightarrow 2OH$ was integrated along lines perpendicular to the quartz walls of the chamber and projected on a plane (Fig. 19).

Some OH-emission is experimentally observed only in the central part of the combustion chamber whereas in the computation, the flame spreads over the

whole domain. Two zones can be evidenced in the simulation : the first one is characterized by a low chemical activity in the recirculation zone and the other by high levels of reaction rate in the axial region of the chamber. This later zone fits well with the experimental images (Fig. 19).

The fact that no OH-emission is recorded by the CCD camera in the recirculation zone during the first 800 μs may be explained by the presence of a very rich mixture in this region (the overall equivalence ratio is about four). Figure 20 presents the maximum values of the reaction rate of the reaction $H_2O + O \leftrightarrow 2OH$ in a laminar flame against the equivalence ratio : at $\phi = 4$, the maximum value of the reaction rate is three orders of magnitude lower than around stoichiometry. This could explain why a OH^*-signal is detected around the axis of the jet where the equivalence ratio is close to one whereas in the rich-recirculation zone the spontaneous OH-chemiluminescence of the flame is not intense enough to be detected by the CCD-camera. This assumption was already made by Schmidt et al [19], from the comparison between Schlieren and OH-emission pictures. As seen on Fig. 21, OH-visualizations and Schlieren photographs do not agree on the flame position and topology. According to OH images the flame kernel keeps a constant diameter during the first 200 μs which is in contradiction with the observation of the Schlieren pictures on Fig. 21a and b. And at 680 μs, the Schlieren image shows a flame front at chamber walls whereas the OH-signal record shows an intense reactive zone on the axis of the jet.

From OH-imaging, Schmidt et al. have tracked the most upstream and downstream flame points (respectively x_u and x_d) during the ignition sequence [19]. These positions have been reported and compared to LES results on Fig. 22, together with the positions extracted from the three Schlieren images. The movement of the downstream point given by the computation is close to the

tracking from Schlieren images but does not match the one based on OH-emission pictures. The poor sensitivity of the CCD camera to the low intensity emission of the flame in rich condition (in the downstream area of the chamber) may be the explanation. For the location of the upstream position a general good agreement is observed. Some differences are observed from 0.2 to 0.4 ms (Fig. 22b), where flame positions extracted from LES and Schlieren pictures are close but do not match OH-imaging tracking. The explanation is that the most upstream flame point propagates at 7 mm off-centre from the jet axis (Fig. 22c) where the mixture is rich and thus is not captured by the CCD camera. On Fig. 22b, the temporal evolution of the upstream position of the flame on the jet axis (x_{axis}) obtained from the LES is close to the position x_u recorded from the OH-images.

6.3 A scenario for ignition

The previous results suggest that ignition is controlled by several phenomena. High levels of turbulence generated in the central jet shear layer enhance mixing wrinkling of the flame front. However, the high-speed jets issuing from the coaxial injector tend to blow out the flame. These phenomena are competing during the different phases of the ignition transient. From OH-imaging, Schmidt et al [19] proposed a flame propagation scenario following four steps : (i) the primary ignition phase, (ii) the upstream propagation of the flame, (iii) the anchoring and the (iv) stabilization phases. This ignition scenario has also been observed by Ahmed and Mastoralos [8,65] in the case of the ignition of a turbulent methane jet by a spark plug and a similar process can be identified in more complex configurations such as gas turbines [66]. In the present case,

this scenario may be refined with the LES results.

(i) The primary ignition phase (from $t = 0$ to $t = 100\ \mu s$)

This phase is characterized by the formation of the flame kernel after the laser shot and ends when the kernel reaches recirculation zones. In the computation this step lasts about 100 μs (Fig. 23 a and b). After the energy deposition, the hot gas kernel is first slowly convected downstream by the jet without stretching. Then at $t \approx 20\ \mu s$ chemical reactions start and as the kernel grows its surface is increasingly wrinkled. The flame zone near the jet axis is transported downstream by the flow whereas the flame zone in the surrounding mixing layer remains quite motionless. During this phase, the success of ignition depends on the competition between heat release, heat transfer, convective and stretching effects [66,16]. At the end of this phase (Fig. 23 b), the flame kernel is no longer a sphere, its upstream central part is wrinkled by the jet turbulence and both side fronts reach the recirculation zone.

(ii) Flame propagation phase (from $t = 100\ \mu s$ to $t = 600 \mu s$)

The kernel phase is followed by a rapid expansion of the flame in the recirculation zone, consuming the partially premixed mixture that fills the chamber (Fig. 23 b to f). The flame development mainly depends on the flow condition : around the jet, hydrogen and oxygen are well mixed and the low velocities leads to the fast flame propagation whereas, the flame zone on the jet axis is convected downstream.

Because the flame propagating in the recirculation zone is not detected with the OH-emission diagnostics, Schmidt et al. concluded that until 400 μs the flame keeps a constant size and is convected downstream [19]. This is true

near the axis but as shown in the previous section, the actual upstream point moves upstream in the recirculation zone (Fig. 22).

At t≈300 μs after ignition, the pressure chamber becomes higher than the H_2-injection dome pressure resulting in an inversion of the flow in the H_2-injection tube. Figure 24 displays the time evolutions of the dome and chamber pressures and the velocity in the H_2-injection pipe. Initially the hydrogen flows in the chamber at 400 m/s but after ignition the velocity drops and becomes negative at 470 μs after the laser shot. It becomes positive again at 1.14 ms just after the chamber pressure peak has been reached. The inversion of the H_2-injection velocity has a direct effect on flame propagation, as shown on Fig. 23 e and f. On the jet axis, the flame front shape and structure are modified : its curvature initially due to high velocity convection (Fig. 23 e) changes as the flow in the H_2 tube inverses (Fig. 23 f) and the most upstream flame zone accelerates towards the injection plate. At $t \approx 580\mu s$, this region of the flame encounters stoichiometric condition in the vicinity of the injection exit and the flame initially burning the mixture in partially premixed regime becomes a triple flame (this aspect will be clearly evidenced in the last section). During this phase, a change in the flame propagation direction is also observed in the experiment and an increase of the intensity of the OH-emission [19] reveals that the flame reaches the stoichiometric (Fig. 23d, e and f).

Figure 22 shows that the upstream and downstream flame points in both LES and experiment (Schlieren) reach the injection plate and the exit nozzle at approximatively the same time (t≈ 0.6 ms).

(iii) Anchoring phase (from $t = 0.6\ ms$ to $t = 1.14\ ms$)

At t ≈0.6 ms, a small diffusion flame settles at the oxygen injection tube and the premixed flame propagating in the recirculation zone consumes the last pockets of unburned mixture trapped at walls (Fig. 23g and h). Until $t = 1.14\ ms$, H_2 injection is stopped and the flame is stabilized between the oxygen flowing from the injector and the hydrogen remaining in the rich burned gases. Note that the injection of oxygen never stops (Fig. 11 as the oxygen dome pressure keeps a constant value of 12 bar, which is above the chamber peak pressure of 11.2 bar). At t=1.1 ms after ignition, all the flammable mixture has burned and the chamber pressure reaches a maximum of 11.2 bar (Fig. 17). The end of this phase is characterized by the fact that hydrogen starts to flow again into the chamber ($t = 1.14\ ms$) and that a "normal" diffusion flame can now stabilize in the last phase.

(iv) Stabilization phase (after $t = 1.14\ ms$)

During the fourth and final phase, in both LES and experiment, the flame stabilizes in a pencil-like shape in the shear layer between the hydrogen and oxygen jets (Fig. 23i). Its influence on the mean chamber pressure is insignificant and it lengthens as the pressure in the vessel decreases.

6.4 Further analysis

Combustion regimes

To determine the flame regime (premixed or/and diffusion) the Takeno index [67] : $\Upsilon = \nabla Y_{O2}.\nabla Y_{H2}$ and the indexed reaction rate : $\dot{\omega}^*_{H2} = \dot{\omega}_{H2}\frac{\Upsilon}{|\nabla Y_{O2}.\nabla Y_{H2}|}$ are used ($\dot{\omega}_{H2}$ is the consumption rate of H_2). When $\dot{\omega}^*_{H2} = +\dot{\omega}_{H2}$ the gradients of the reactants have the same sign and the flame is premixed ; otherwise

($\dot{\omega}^*_{H2} = -\dot{\omega}_{H2}$) the flame is a diffusion flame. Figure 25 presents four computed snapshots of $\dot{\omega}^*_{H2}$ at four different times of the "kernel-propagation", "anchoring" and "stabilization" phases. The propagation of the flame in the recirculation zone is purely premixed (Fig. 25a), but near the jet axis, when approaching the injection tube, a triple flame appears with two lean and rich branches and a diffusion flame in between along the stoichiometric line (Fig. 25b). The anchoring phase (Fig. 25c) is characterized by a diffusion flame at the injector while pockets of flammable mixture trapped at walls are consumed in premixed mode. At the end of the computation, the flame stabilizes in a pure diffusion regime at the injector lips, between the hydrogen and oxygen jets (Fig. 25d). This ignition process is substantially different from a classical turbulent jet ignition observed for example in the experiment of Ahmed and Mastorakos [8,65] where the flame only propagates in the jet mixing layer, first as a partially premixed flame and then as a triple flame.

Propagation processes

To identify the processes controlling the flame expansion during the "kernel" and "propagation" phases, two speeds can be defined [1] :

- the absolute flame speed V_f, corresponding to the front speed relative to a fixed reference frame. V_f is estimated from an equivalent spherical flame with a volume equal to the burned gas volume :

$$V_f = \frac{dr}{dt} \tag{11}$$

[1] Another speed, the displacement speed S_d, is sometimes used for perfectly spherical flames : $S_d = \rho_b g / \rho_u g . dr/dt$ [68,24] ($\rho_b g$ and $\rho_u g$ are respectively the density of the burned and unburned gases). This expression is not adapted to diffusion flames and is not used for the present study.

where r is the radius of the equivalent spherical flame, $r = \left(\frac{3}{4\pi}V_{bg}\right)^{1/3}$ and V_{bg} is the volume of the burned gas directly measured during the computation.

- the consumption speed $< S_c >$ that characterizes the speed at which the reactants are consumed. $< S_c >$ is calculated from the consumption rate of the oxygen :

$$< S_c >= -\frac{\int \dot{\omega}_{O_2} dv}{\rho_{ug} Y_{O_2} \Sigma_{sphere}} \tag{12}$$

where $\dot{\omega}_{O_2}$ is the consumption rate of O_2, ρ_{ug} the density of the unburned gas, Y_{O_2} the mass fraction of O_2 assumed constant in the cold mixture ($Y_{O_2} \approx 0.666$) and Σ_{sphere} the surface of the equivalent sphere of burned gases.

Figure 26 compares the two quantities V_f and $< S_c >$. The resolved flame area shown on Fig. 27 decreases after 0.5 ms, corresponding to the time when the flame interacts with the walls and is no longer a closed surface. Therefore, the flame speed curves of Fig. 26 are relevant only for $t < 0.5ms$. The consumption speed $< S_c >$ is rather constant and close to 14 m/s which is about 3 times the laminar flame speed S_l^0 (at $\phi = 4$ and $P = 2bar$, $S_l^0 = 4.71m/s$), corresponding to the ratio between the real wrinkled flame surface (Σ_{real}) and the area of the equivalent spherical flame (Σ_{sphere}) :

$$\frac{< S_c >}{S_l^0} = \frac{\Sigma_{real}}{\Sigma_{sphere}} = \frac{\Sigma_{real}}{\Sigma_{res}} \frac{\Sigma_{res}}{\Sigma_{sphere}} \tag{13}$$

In Eq. 13 the first term $\frac{\Sigma_{real}}{\Sigma_{res}}$ represents the sub-grid scale wrinkling of the flame, modeled by the combustion model (TFLES) by the efficiency function [44] and the second term $\frac{\Sigma_{res}}{\Sigma_{sphere}}$ is the resolved wrinkling of the flame.

The temporal evolution of these two quantities are presented on Fig. 27c where the global wrinkling $\frac{\Sigma_{real}}{\Sigma_{sphere}}$ is mainly due to the sub-grid scale wrinkling : the resolved flame is moderately corrugated with a resolved wrinkling of the order of 1.35. The product of the resolved and the sub-grid scale wrinkling is about 3, which corresponds well to the ratio $< S_c > /S_l^0$.

V_f is nearly one order of magnitude higher than $< S_c >$ with an average value of 65 m/s. The slight decrease of V_f may be caused by confinement effects. The ratio of the absolute flame speed V_f to the consumption speed $< S_c >$ is approximatively equal to 5. The theory on premixed spherical flame propagation [24] gives $V_f / < S_c >= \rho_{ug}/\rho_{bg}$ (with ρ_{bg} and ρ_{ug} the density of burned and unburned gases). In the present case, $\rho_{ug}/\rho_{bg} \approx 5.3$ which indicates that the flame propagation mechanism during the "kernel" and the "propagation" phases correspond to a turbulent spherical flame process with a significant effect of hot gas expansion.

7 Conclusions

A compressible LES methodology to compute flame ignition and propagation in a rocket engine fueled by gaseous oxygen and hydrogen has been established and tested in the M3 configuration of DLR [19]. Results from LES are in good agreement with experimental observations, showing that the simulation captures the right mechanisms for flame ignition, propagation and stabilisation. A six-species, seven-step chemical scheme is used for H_2/O_2 combustion and LES results show that the CCD camera employed to record the spontaneous OH-emission locates properly the flame in the jet region where the equiva-

lence ratio is close to one but has some difficulties to detect the reactive front in the very rich mixture of the recirculation zone. This results in a different interpretation of experimental observations.

The analysis of numerical results and the comparison with experimental data have allowed to establish an ignition scenario and to identify the most important physical phenomena of the process. LES results show that in the early times, the flame expands as a premixed turbulent spherical flame. Then due to an increase of the chamber pressure, the flow direction changes in the hydrogen line making the upstream flame front accelerate towards the injector. At this time, this front enters the shear layer and a diffusion flame attaches at the injector lips, while the premixed flames consume the flammable mixture trapped at walls. At the injector, oxygen does not burn with the injected hydrogen (due to back-flow) but with the hydrogen remaining in the burned gases resulting from the combustion of the initial rich mixture. Once all the fresh mixture has burned, the chamber pressure reaches a maximum of 11.2 bar, close to the experimental measurement (11.1 bar). Finally, hydrogen flows again in the chamber and a standard diffusion flame can stabilize at the injector in a pencil-like shape.

The present delayed ignition results in a chamber full of flammable mixture at ignition time. In the first time after ignition, it has been shown that the flame propagates as a turbulent spherical flame. This well known process studied in premixed ignition [1–3] and in IC engines [69] is more hazardous for ignition in rocket engines because it leads to fast flame propagation and to a strong pressure peak in the chamber. The present approach is now extended to two-phase flow (Euler-Euler) simulations to take into account effects of the liquid phase on the ignition.

8 Acknowledgments

This work was sponsored by the French Space Agency CNES and the prime contractor for the European launcher Ariane 5 cryogenic propulsion systems : Snecma (Safran group). The authors also gratefully acknowledge the computing center CINES where most of the calculations were performed, as well as DLR for fruitful discussions.

References

[1] F. Williams, *Combustion theory*, Benjamin Cummings, Menlo Park, CA, 1985.

[2] I. Glassman, *Combustion*, Academic Press, New York, 1987.

[3] M. Champion, B. Deshaies, G. Joulin, K. Kinoshita, *Combustion and Flame* 65 (1986) 319–337.

[4] V. Kurdyumov, J. Blasco, A. Sanchez, A. Linan, *Combustion and Flame* 136 (2004) 394–397.

[5] M. Champion, B. Deshaies, G. Joulin, *Combustion and Flame* 74 (1988) 161–170.

[6] D. Ballal, A. Lefebvre, *Proceedings of the Royal Society of London. Series A* 357 (1977) 163–181.

[7] M. Baum, *Etude de l'allumage et de la structure des flammes turbulentes*, Ph.d, Ecole Centrale Paris (1994).

[8] S. Ahmed, E. Mastorakos, *Combustion and Flame* 146 (1-2) (2006) 215–231.

[9] S. Ahmed, R. Balachandran, T. Marchione, E. Mastorakos, *Combustion and Flame* 151 (2007) 366–385.

[10] D. Ballal, A. Lefebvre, *Proceedings of the Royal Society of London. Series A* 364 (1978) 277–294.

[11] A. Danis, *Spark Ignition of Monodisperse Fuel Sprays*, Ph.D. thesis, Drexel University, Philadelphia, PA (1987).

[12] K. McManus, F. Aguerre, B. Yip, S. Candel, *Analysis of the ignition sequence of a nonpremixed combustor using PLIF imaging*, Begell House, New York, 1993, pp. 714–725.

[13] W. Mayer, B. Ivancic, A. Schik, U. Hornung, *Journal of Propulsion and Power* 17 (4) (2001) 794–799.

[14] V. Schmidt, D. Klimenko, O. Haidn, M. Oschwald, A. Nicole, G. Ordonneau, M. Habiballah, *ONERA, TP no. 2004-49* 2004 (49).

[15] V. Schmidt, U. Wepler, O. Haidn, M. Oschwald, *42 nd AIAA Aerospace Sciences Meeting and Exhibit* (AIAA-2004-1167).

[16] O. Gurliat, V. Schmidt, O. Haidn, M. Oschwald, *Aerospace Science and Technology* 7 (7) (2003) 517–531.

[17] M. De Rosa, J. Sender, H. Zimmermann, M. Oschwald, *42 nd AIAA Joint Propulsion Conference & Exhibit* (AIAA-2006-4539).

[18] S. Karl, K. Hannemann, in: *3rd International Workshop on Rocket Combustion Modeling (Paris)*, 2006.
URL `http://elib.dlr.de/43913`

[19] V. Schmidt, D. Klimenko, M. Oschwald, *Preliminary results of test case "A" laser ignition tests for coaxial GH2/GO2-Injection*, Tech. Rep. DLR-RA-TE-LI-RP-004, DLR, Lampoldshausen (2003).

[20] P. Moin, K. Squires, W. Cabot, S. Lee, *Physics of Fluids* A 3 (11) (1991) 2746–2757.

[21] M. Lesieur, O. Metais, *Annual Review of Fluid Mechanics* 28 (1996) 45 – 82.

[22] M. Lesieur, in: O. Métais, J. Ferziger (Eds.), New tools in turbulence modelling, Les Editions de Physique - Springer Verlag, 1997, pp. 1 – 28.

[23] H. Pitsch, *Annual Review of Fluid Mechanics* 38 (2006) 453–482.

[24] T. Poinsot, D. Veynante, *Theoretical and numerical combustion*, R.T. Edwards, 2nd edition., 2005.

[25] J. Janicka, A. Sadiki, *Proceedings of the Combustion Institute* 30 (2004) 537–547.

[26] M. Freitag, J. Janicka, *Proceedings of the Combustion Institute* 31 (2007) 1477–1485.

[27] L. Selle, G. Lartigue, T. Poinsot, R. Koch, K.-U. Schildmacher, W. Krebs, B. Prade, P. Kaufmann, D. Veynante, *Combustion and Flame* 137 (4) (2004) 489–505.

[28] F. Di Mare, W. P. Jones, K. Menzies, *Combustion and Flame* 137 (2001) 278–295.

[29] P. Schmitt, T. Poinsot, B. Schuermans, K. Geigle, *Journal of Fluid Mechanics* 570 (2007) 17–46.

[30] M. Boileau, G. Staffelbach, B. Cuenot, T. Poinsot, C. Bérat, *Combustion and Flame* 154 (1) (2008) 2–22.

[31] J. C. Oefelein, *41st Aerospace Sciences Meeting and Exhibit* (AIAA-2003-0479).

[32] J. C. Oefelein, *Proceedings of the Combustion Institute* 30 (2) (2005) 2929–2937.

[33] M. Masquelet, *Simulations of a Sub-scale Liquid Rocket Engine: Transient Heat Transfer in a Real Gas Environment*, Ph.D. thesis, School of Aerospace Engineering Georgia Institute of Technology (December 2006).

[34] M. Barrère, A. Jaumotte, B. F. de Veubeke, J. Vandenkerckhove, *Rocket Propulsion*, Elsevier, 1960.

[35] D. Huzel, D. Huang, *Progress in Astronautics and Aeronautics, AIAA, Washington, DC* 147 (1992) 20.

[36] V. Yang, M. Habiballah, J. Hulka, M. Popp, *Liquid Rocket Thrust Chambers: Aspects of Modeling, Analysis, and Design*, Vol. 200, American Institute of Aeronautics and Astronautics, 2004.

[37] V. Moureau, G. Lartigue, Y. Sommerer, C. Angelberger, O. Colin, T. Poinsot, *Journal of Computational Physics* 202 (2) (2005) 710–736.

[38] R. A. Baurle, S. Girimaji, *Combustion and Flame* 134 (2003) 131–148.

[39] P. D. Lax, B. Wendroff, *Communications on pure and applied mathematics* 17 (1964) 381–398.

[40] J. Smagorinsky, *Monthly Weather Review* 91 (1963) 99–164.

[41] T. Poinsot, S. Lele, *Journal of Computational Physics* 101 (1) (1992) 104–129.

[42] C. Martin, L. Benoit, Y. Sommerer, F. Nicoud, T. Poinsot, *AIAA Journal* 44 (4) (2006) 741–750.

[43] A. Sengissen, A. Giauque, G. Staffelbach, M. Porta, W. Krebs, P. Kaufmann, T. Poinsot, *Proceedings of the Combustion Institute* 31 (2007) 1729–1736.

[44] O. Colin, F. Ducros, D. Veynante, T. Poinsot, *Physics of Fluids* 12 (7) (2000) 1843–1863.

[45] C. Angelberger, F. Egolfopoulos, D. Veynante, *Flow, Turbulence and Combustion* 65 (2) (2000) 205–22.

[46] P. Thompson, *Compressible-fluid dynamics*, McGraw-Hill, 1972.

[47] A. W. Cook, W. H. Cabot, *Journal of Computational Physics* 203 (2005) 379–385.

[48] C. Hirsch, *Numerical Computation of internal and external flows*, John Wiley, New York, 1988.

[49] B. Fiorina, S. Lele, *Journal of Computational Physics* 222 (1) (2007) 246–264.

[50] R. Maly, *Proceedings of the Combustion Institute* 18 (1981) 1747–1754.

[51] S. Pischinger, J. Heywood, *Proceedings of the Combustion Institute* 23 (1990) 1033–1040.

[52] P. Boudier, S. Henriot, T. Poinsot, B. T., *Proceedings of the Combustion Institute* 24 (1992) 503–510.

[53] T. Kravchik, E. Sher, *Combustion and Flame* 99 (1994) 635–643.

[54] D. Bradley, F. Lung, *Combustion and Flame* 69 (1) (1987) 71–93.

[55] C. Vázquez-Espí, A. Liñán, *Combustion Theory and Modelling* 6 (2) (2002) 297–315.

[56] N. Chakraborty, R. S. Mastorakos, E. Cant, *Combustion Science and Technology* 179 (1-3) (2007) 293–317.

[57] D. Bradley, C. Sheppard, I. Suardjaja, R. Woolley, *Combustion and Flame* 138 (2004) 55–77.

[58] T. Phuoc, F. White, *Proceedings of the Combustion Institute* 29 (2002) 1621 – 1628.

[59] V. Erard, A. Boukhalfa, D. Puechberty, M. Coria-Ura, *Combustion Science and Technology* 113 (1) (1996) 313–327.

[60] M. O'Conaire, H. Curran, J. Simmie, W. Pitz, C. Westbrook, *International Journal of Chemical Kinetics* 36 (11) (2004) 603–622.

[61] R. Kee, J. Warnatz, J. Miller, *A fortran computer code package for the evaluation of gas phase viscosities, conductivities, and diffusion coefficients*, Tech. Rep. SAND83-8209, Sandia National Laboratories (1983).

[62] M. Smooke, M. Koszykowski, *Fully adaptive solutions of one-dimensional mixed initial-boundary value problem with applications to unstable problems in combustion*, Tech. Rep. SAND 83-8219, Sandia National Laboratories (1983).

[63] D. Panara, M. Porta, R. Dannecker, B. Noll, in: *Proceedings of the 5th International Symposium on Turbulence, Heat and Mass Transfer.*, 2006.

[64] A. H. Shapiro, *The Dynamics and Thermodynamics of Compressible Fluid Flow*, Wiley, 1953.

[65] E. Mastorakos, *Progress in Energy and Combustion Science* 35 (2009) 57–97.

[66] A. Lefebvre, *Gas Turbines Combustion*, Taylor & Francis, 1999.

[67] H. Yamashita, M. Shimada, T. Takeno, *Proceedings of the Combustion Institute* 26 (1996) 27 – 34.

[68] D. Dowdy, D. Smith, S. Taylor, *Proceedings of the Combustion Institute* 23 (1990) 325–332.

[69] J. Heywood, *Internal combustion engine fundamentals*, McGraw and Hill Series in Mechanical Engineering, McGraw-Hill, New-York, 1988.

9 Tables

cold flow	O_2	1.135
mass flux [g/s]	H_2	0.592
Dome total	O_2	300
temperature [K]	H_2	302
Dome total	O_2	11.7
Pressure [bar]	H_2	2.1
Pressure of the chamber [bar]		1.87

Table 1

Injection conditions for the M3 test case (at ignition time).

N2 valve closure : t_{N2}	-1000ms
H_2 valve opening : t_{H2}	0 ms
O_2 valve opening : t_{O2}	7 ms
laser ignition : $t_{ignition}$	370 ms

Table 2

Time sequence for the M3 test case.

Reaction	**A**	β	**Ea**
	[cm^3/mole.sec]		**[cal/mole]**
$H + O_2 = O + OH$	3.62E+17	-0.91	1.653E+4
$O + H_2 = H + OH$	1.53E+5	2.67	6.296E+3
$O_2 + H_2 = OH + OH$	5.13E+13	0.00	4.805E+4
$OH + H_2 = H_2O + H$	6.64E+13	0.00	5.155E+3
$OH + OH = H_2O + O$	1.90E+13	0.00	1.091E+3
$H + OH + M = H_2O + M$	6.67E+22	-2.00	0.000
$H + H + M = H_2 + M$	2.20E+18	-1.00	0.000
third body efficiencies :			
2.5 for H_2, 16 for H_2O and 1.0 for all other M			
Schmidt numbers :			
H_2 : 0.28 ; O_2 : 0.99 ; H_2O : 0.77 ; H : 0.17 ; O : 0.64 ; OH : 0.65			

Table 3

The seven-step H_2-O_2 kinetic scheme.

List of Figures

10 Figures

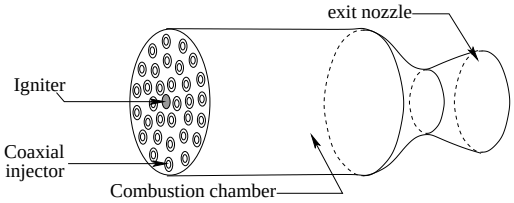

Fig. 1. Sketch of a real combustion chamber.

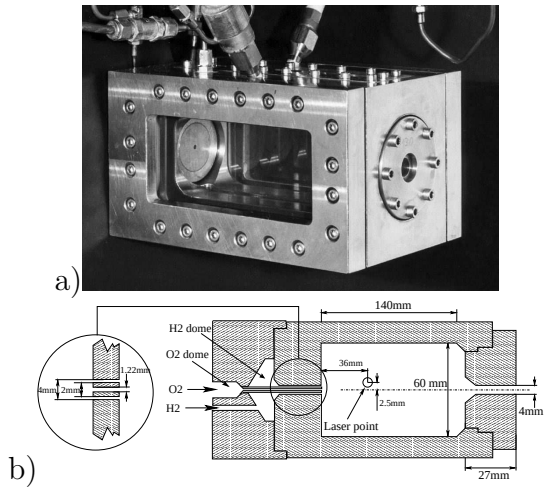

Fig. 2. The Micro-Combustor M3. a) Photograph. b) Geometry [19].

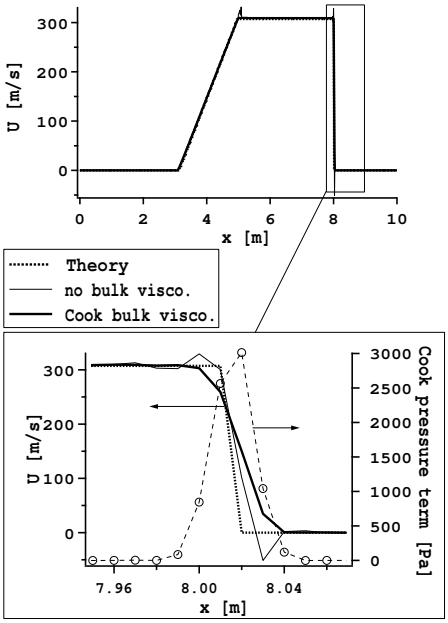

Fig. 3. Velocity profiles in a shock tube problem 5 ms after diaphragm breakdown: comparison between theory and results obtained with and without the approach of Cook [47].

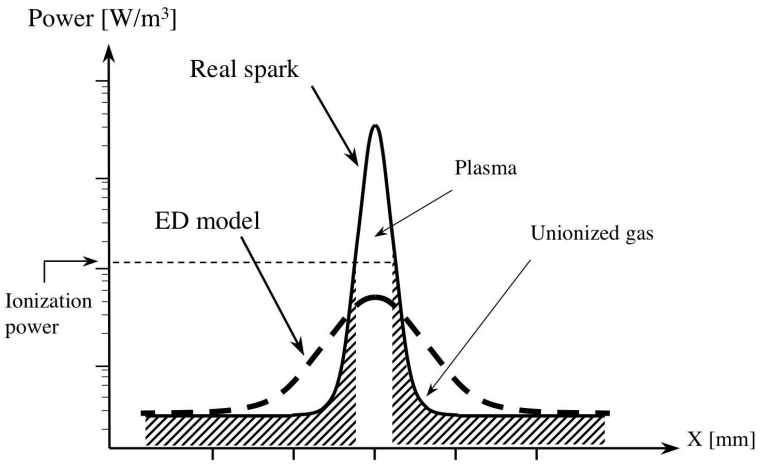

Fig. 4. Sketch of power distribution inside a spark kernel and part of the flow modeled with the ED model. The ED model reproduces the effect of the spark from the time when the temperature of the kernel has decreased below the ionization temperature.

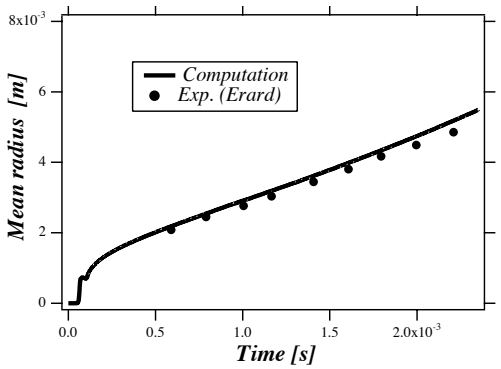

Fig. 5. Temporal evolution of the radius of a laminar spherical flame ignited by an electrical spark in a propane-air mixture at ϕ=1 and 1 bar. Line : computation, symbols : experimental results from Erard et al. [59].

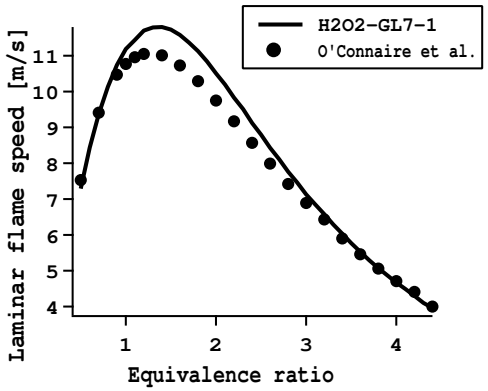

Fig. 6. Chemical comparison of the laminar flame speed given by the seven-step scheme (H2O2-GL7-1) used for the computation and a detailed chemistry from O'Conaire et al. [60] ($T_{cold\ gas} = 300K$ P=2.0 bar).

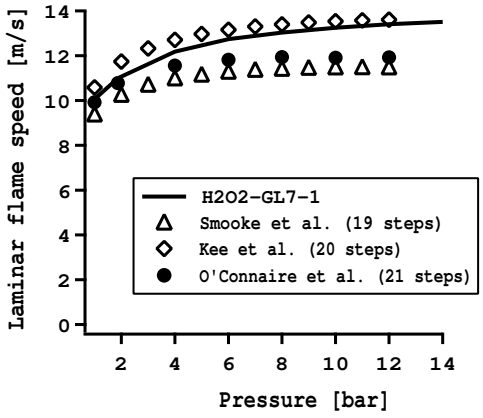

Fig. 7. Laminar flame speed against pressure, comparison between the seven-step scheme (H2O2-GL7-1) and three detailed chemistries from O'Conaire et al. [60], Smooke et al. [62] and Kee et al. [61] ($T_{cold\ gas} = 300K$, $\phi = 1.0$).

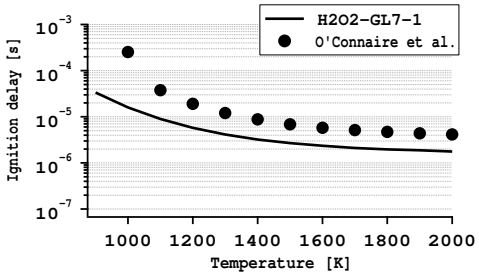

Fig. 8. Ignition delay, comparison between the seven-step scheme (H2O2-GL7-1) and the detailed chemistry from O'Conaire et al. [60] (homogeneous ignition at constant volume for an equivalence ratio of 1.0 and an initial pressure of 1 bar).

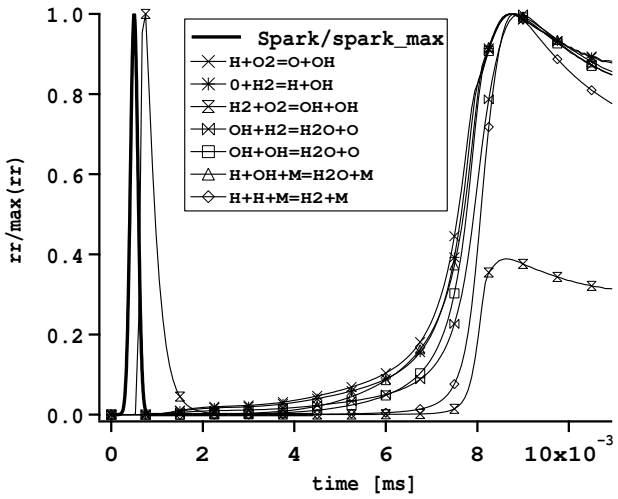

Fig. 9. Chemical path initiated after energy deposition in a 1D configuration ($H_2 - O_2$ mixture at $\phi = 4$, P=2 bar and T=300 K and duration of the deposition: 500 ns). Test realized with the H2O2-GL7-1 scheme, each reaction rate rr is scaled by its maximum value.

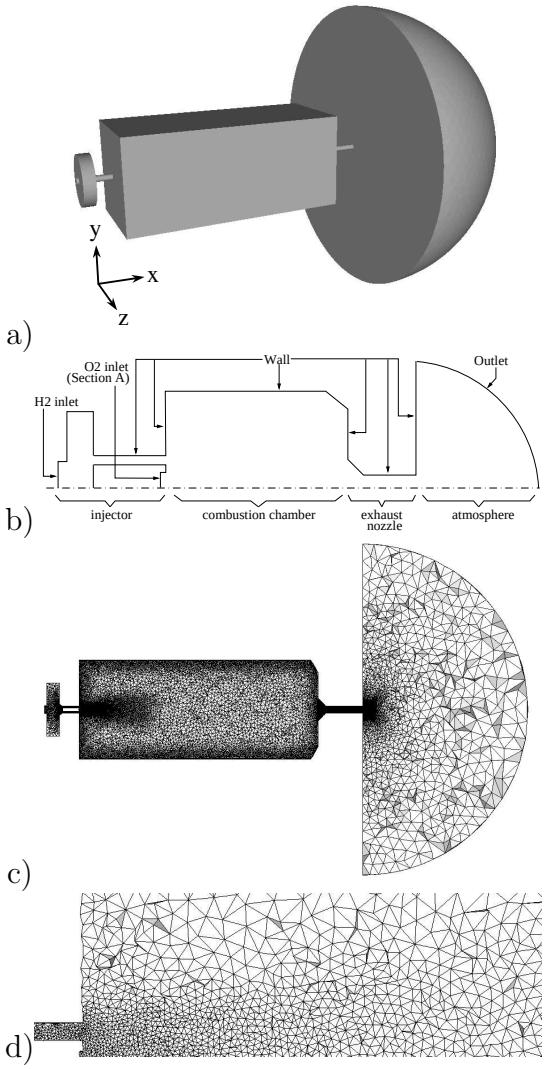

Fig. 10. Computing domain for the M3 Micro-combustor. a) Geometry, b) Sketch of boundary conditions, c) mesh, d) zoom around the inlet region.

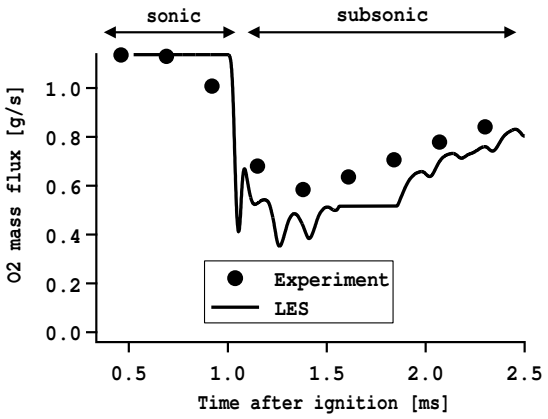

Fig. 11. Temporal evolution of the oxygen injection mass flux compared to the experiment.

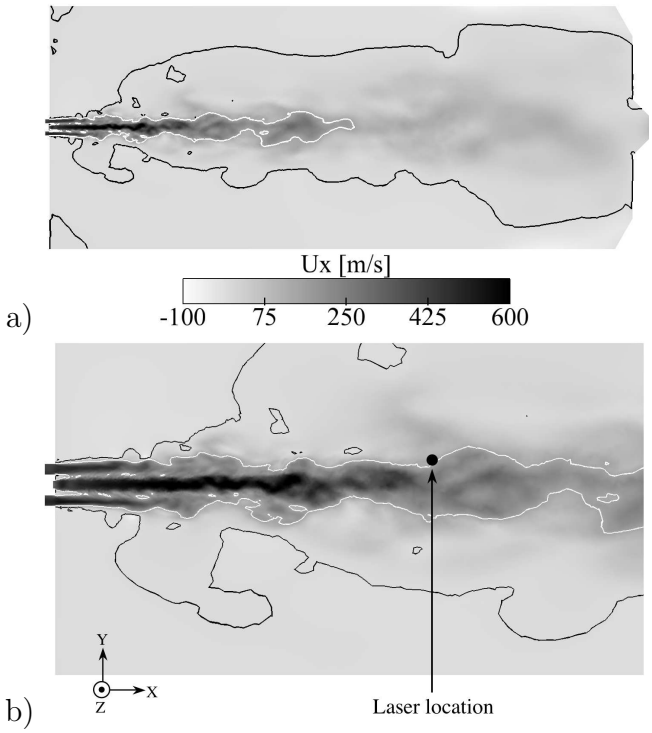

Fig. 12. Axial velocity field at ignition time : (a) whole chamber, (b) near-injector region (black line : 0 m/s, white line : 150 m/s) .

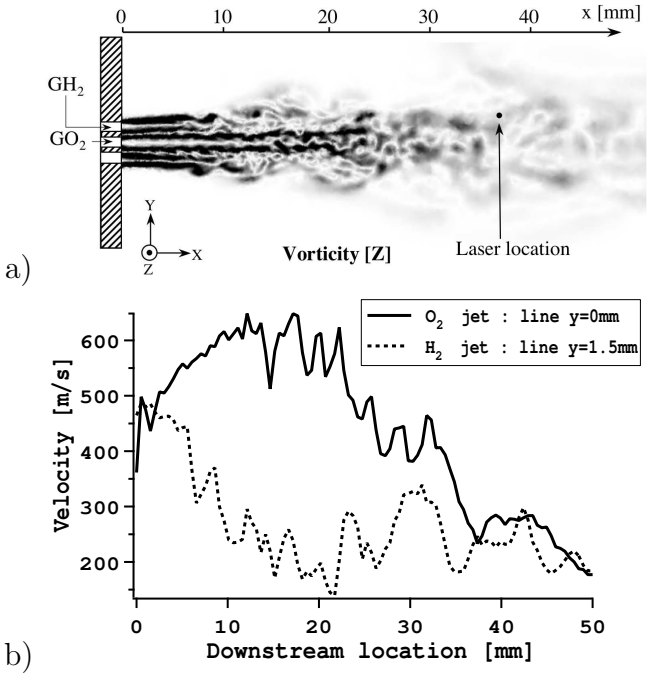

Fig. 13. Jets interaction : (a) Vorticity field, (b) velocity along the O_2 and the H_2 jet axis.

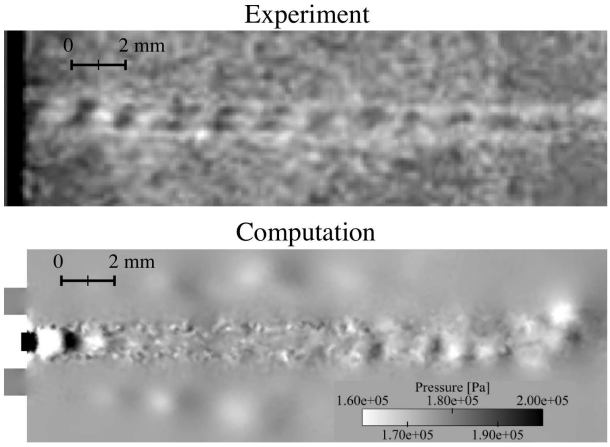

Fig. 14. Comparison of the jet topology at the injector exit between the experiment (Schlieren picture) and the LES (instantaneous pressure field).

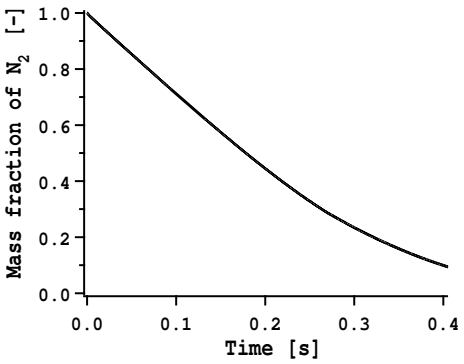

Fig. 15. Temporal evolution of the computed mean mass fraction of nitrogen in the chamber during the injection phase. At ignition time (t=370 ms) $Y_{N_2} = 0.14$.

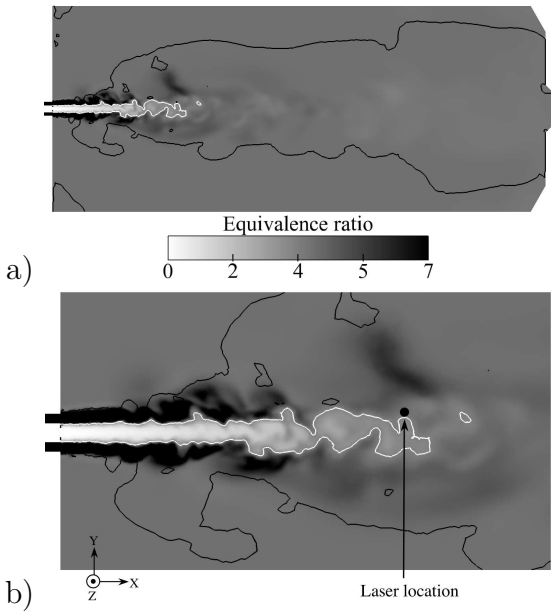

Fig. 16. Field of equivalence ratio (ϕ) at ignition time : (a) cut of the whole chamber, (b) detail of the jet region (black line : 0 m/s , white line : $\phi = 3$).

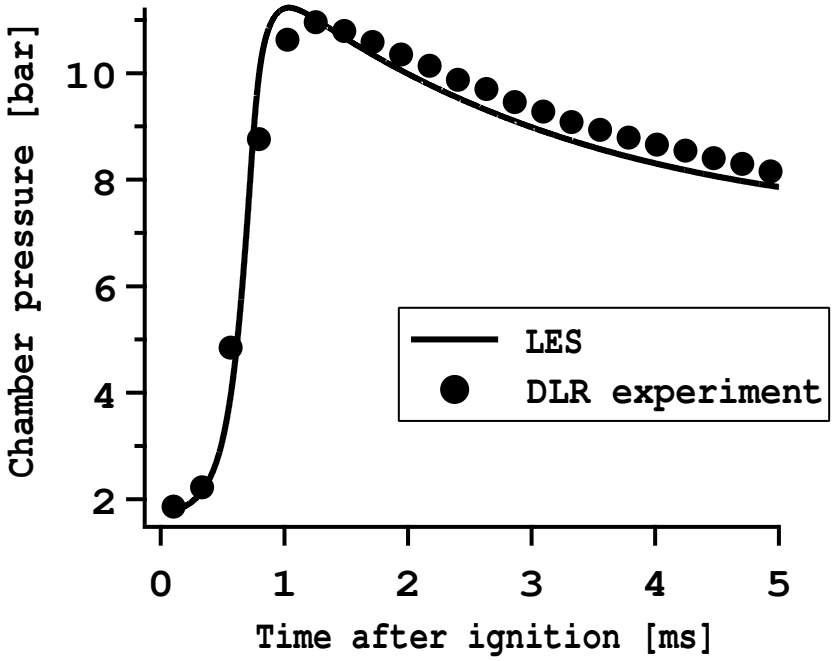

Fig. 17. Time evolution of the chamber pressure : LES vs Experiment.

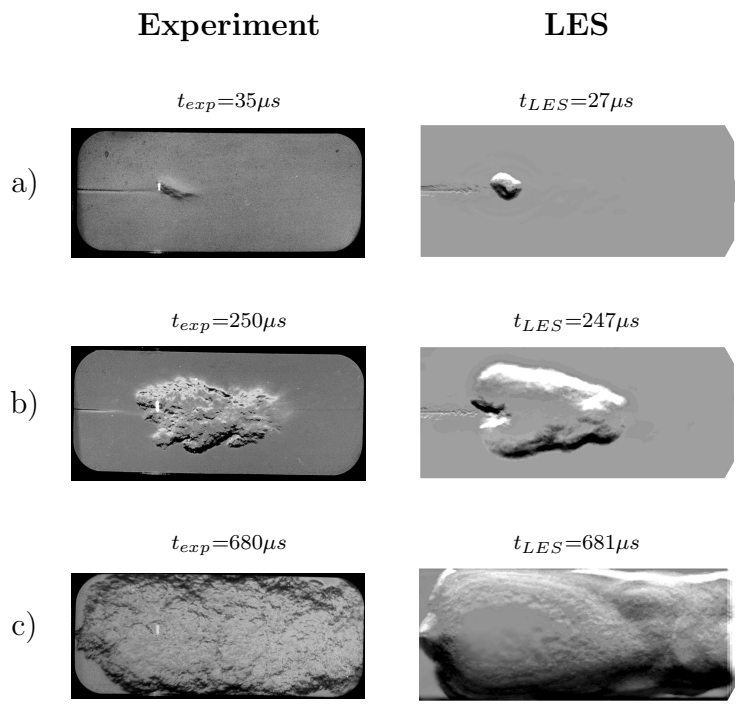

Fig. 18. Comparison of Schlieren pictures [19] and LES fields of the density gradient (integrated in the width of the chamber) at three different times after ignition.

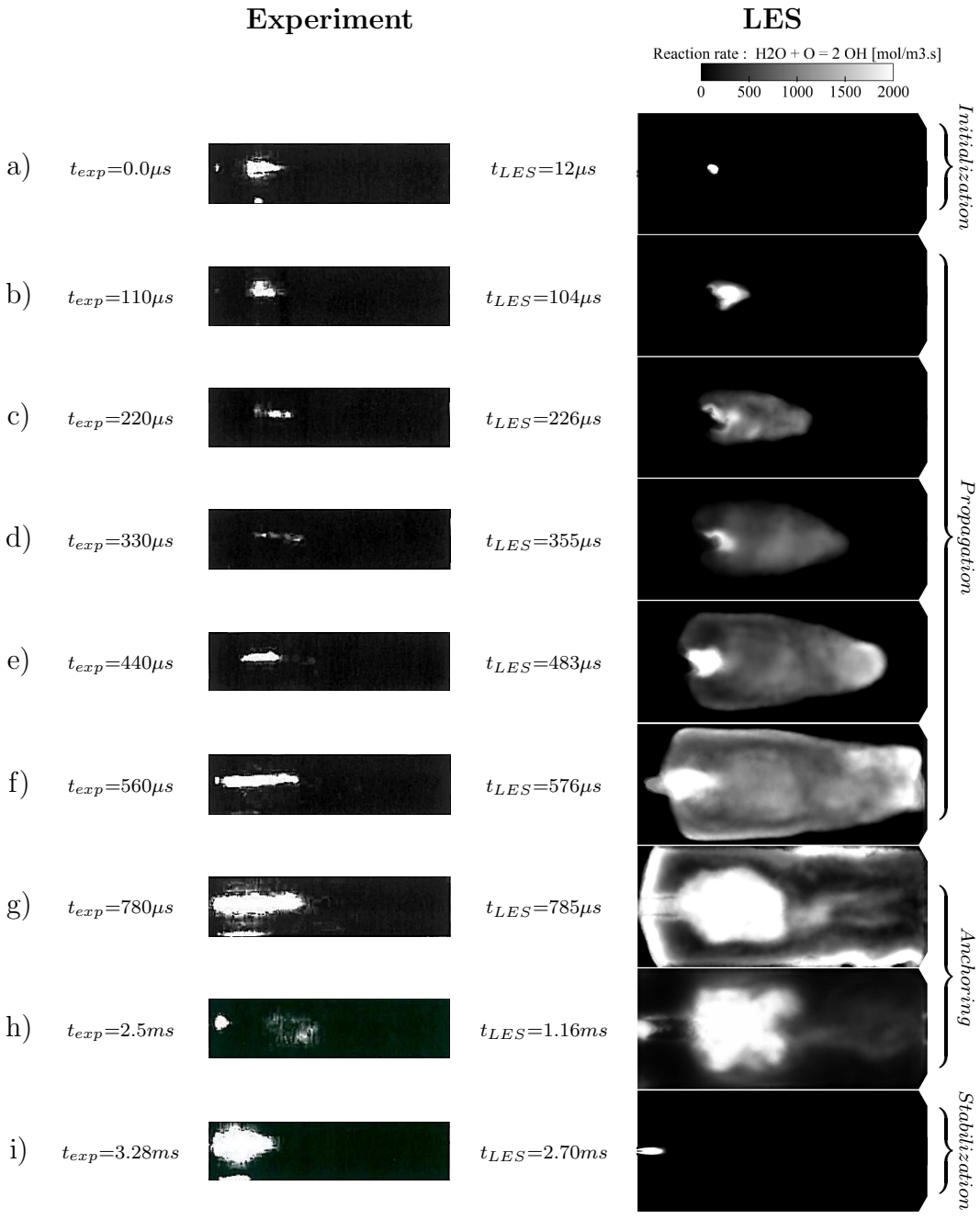

Fig. 19. Experimental OH-emission images compared to integrations across the chamber of the reaction rate of $H_2O + O \leftrightarrow OH + OH$.

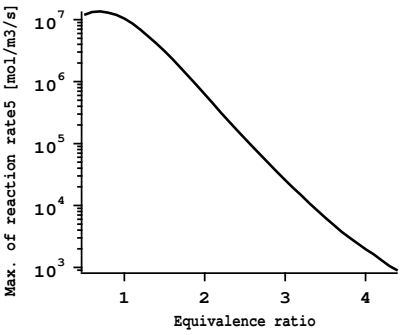

Fig. 20. Maximum of the reaction rate of the reaction $H_2O + O \leftrightarrow 2OH$ (reaction 5 in the H2O2-GL7-1 scheme) in laminar flames at different equivalence ratio given by the chemical scheme used in the present LES (To = 300 K and P = 1 bar).

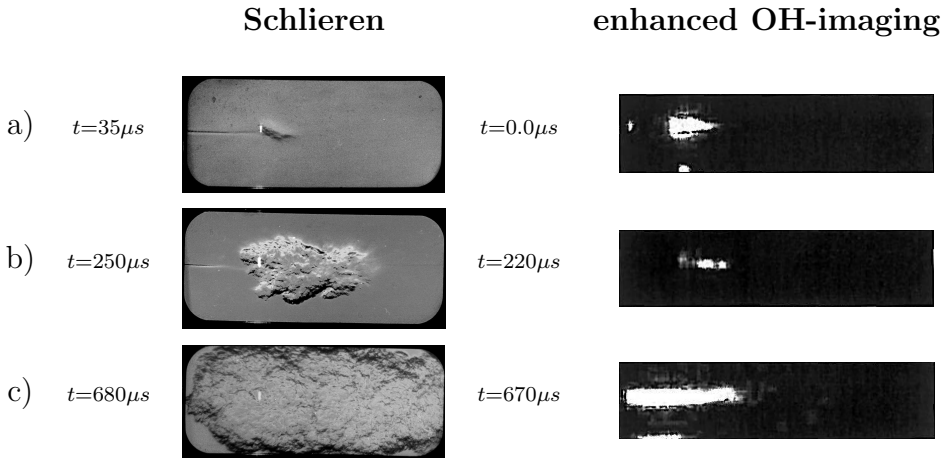

Fig. 21. Comparison of Schlieren pictures and enhanced OH-emission images at three different times after ignition [19].

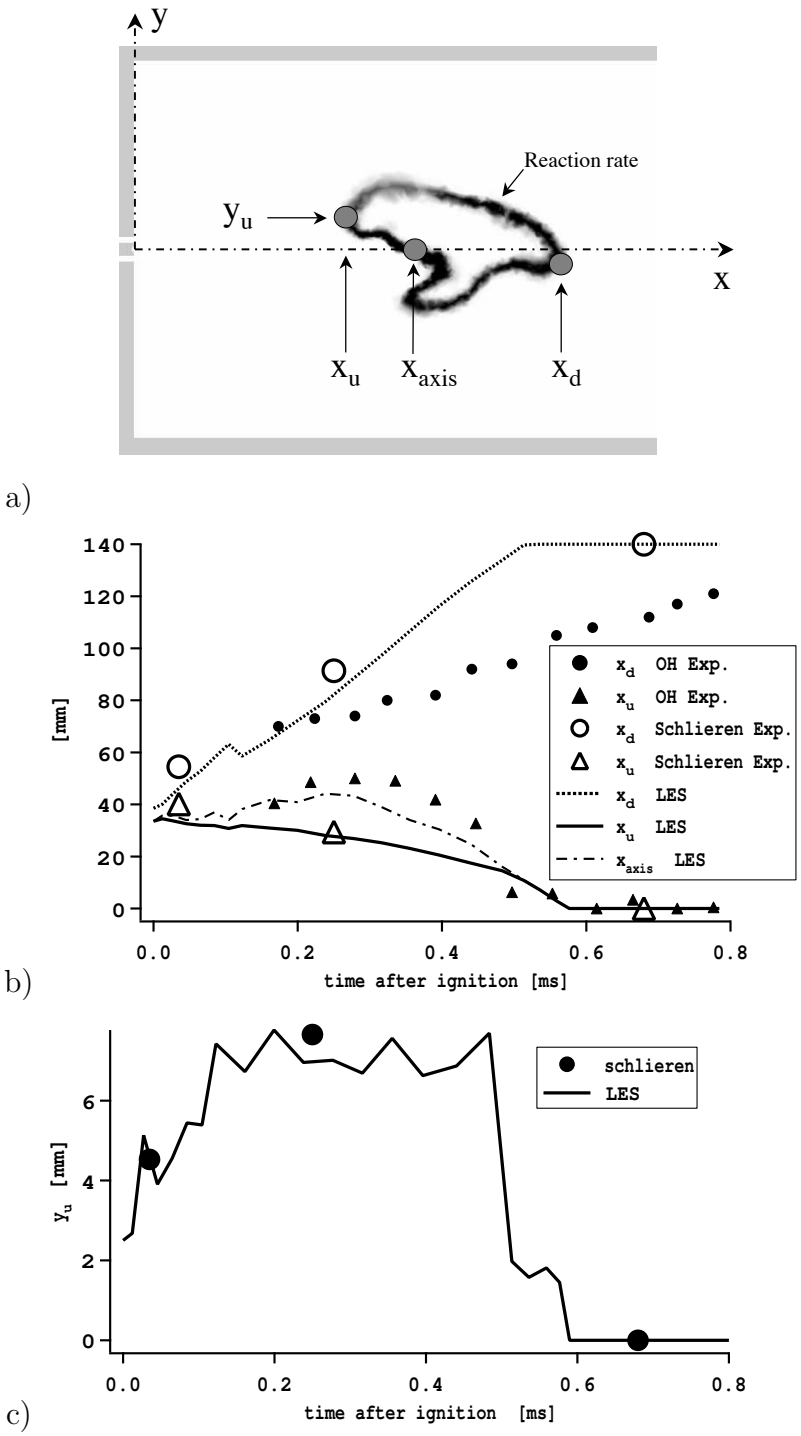

Fig. 22. Position of the most upstream and most downstream flame points during the ignition transient. a) Sketch of the different flame position measurements. b) comparison of the most upstream and downstream flame positions (respectively x_u and x_d) and the flame position on the axis of the jet (x_{axis}) between experiment [19] and LES. c) transversal position (y_u) of the most upstream flame point.

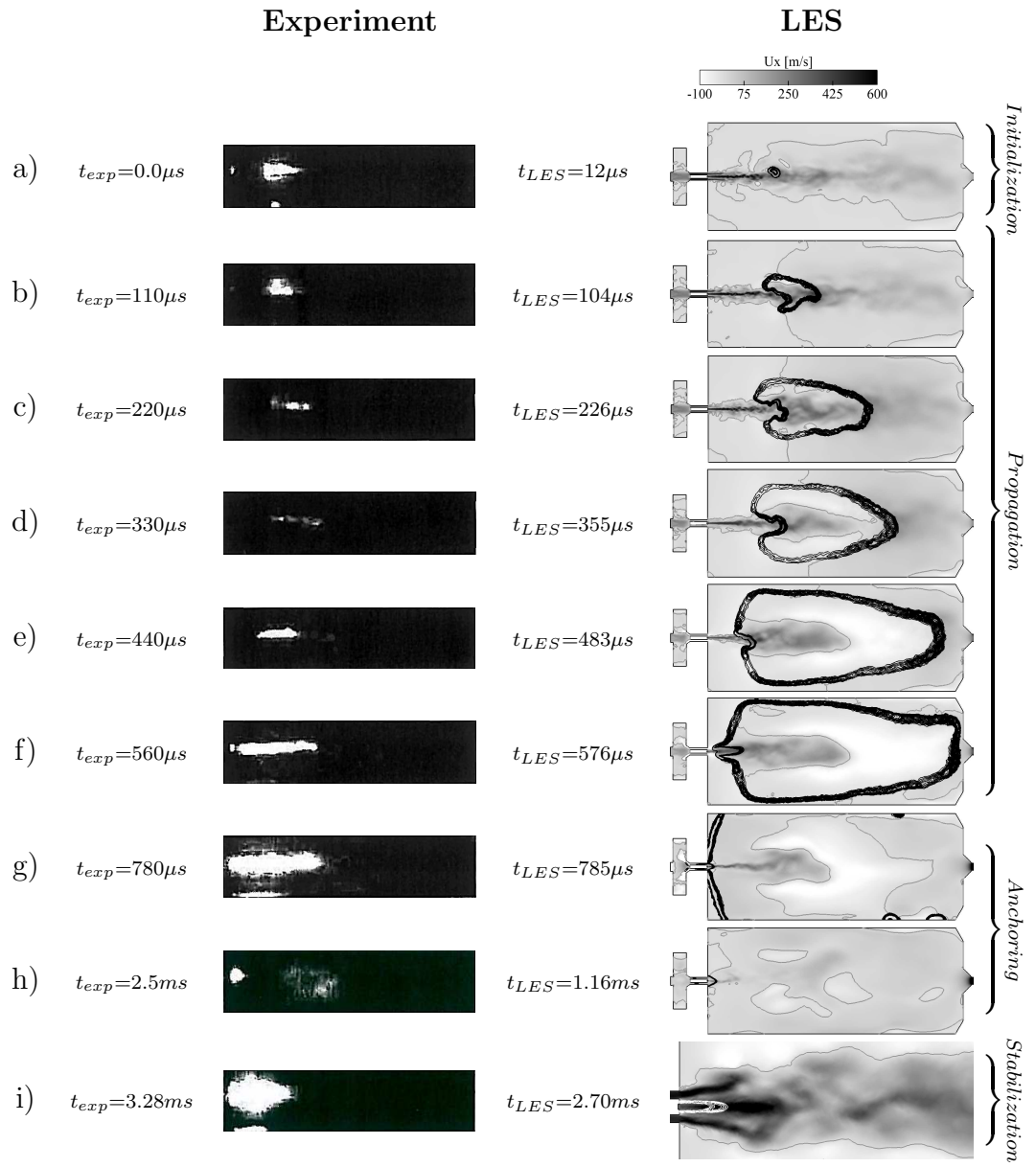

Fig. 23. Experimental OH-emission images and LES axial-velocity field (Ux) in the centerplane (black iso-line : reaction rate of $H_2O + O \leftrightarrow OH + OH$, grey iso-line : $Ux = 0\ m/s$). Note : for the last LES results ($t_{LES} = 2.7ms$) the reaction rate is located by white iso-lines.

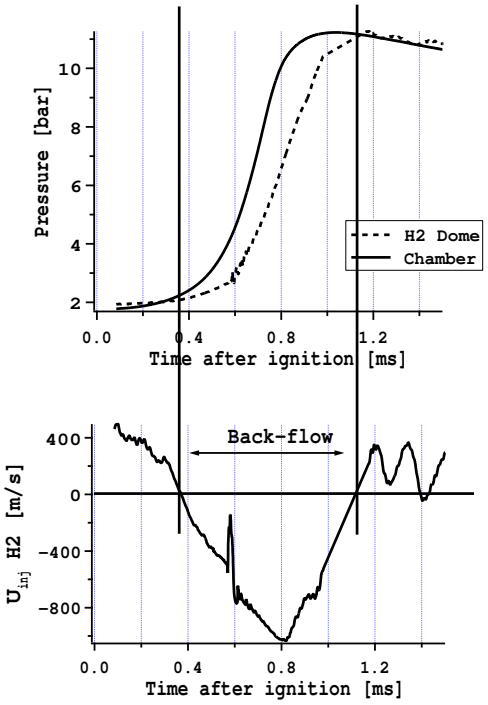

Fig. 24. The back-flow in hydrogen injection line : pressure traces in the chamber and in the H_2 injection dome and axial velocity in the H_2 injection tube.

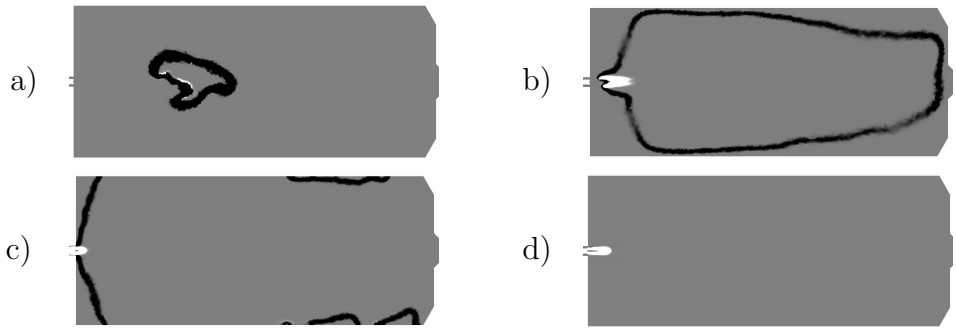

Fig. 25. Flame regimes : snapshots of the indexed reaction rate $\dot{\omega}^*_{H2}$ (black = premixed flame, white = diffusion flame). a) $t = 124\mu s$, b) $t = 577\mu s$, c) $t = 737\mu s$ and d) $t = 2.7ms$.

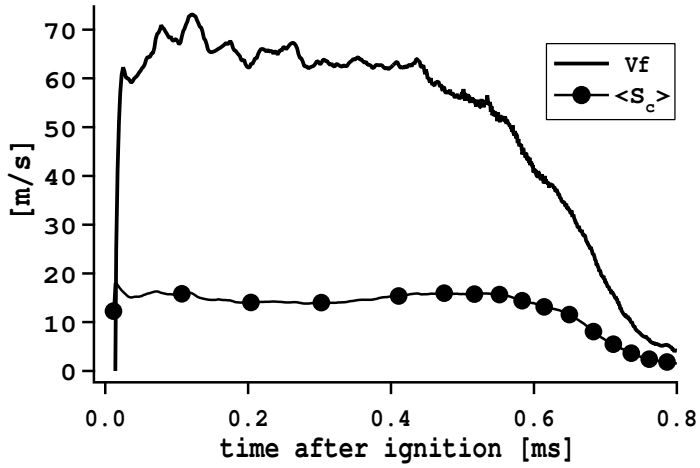

Fig. 26. Comparison between the absolute front speed V_f and the mean consumption speed $< S_c >$ during the "propagation phase".

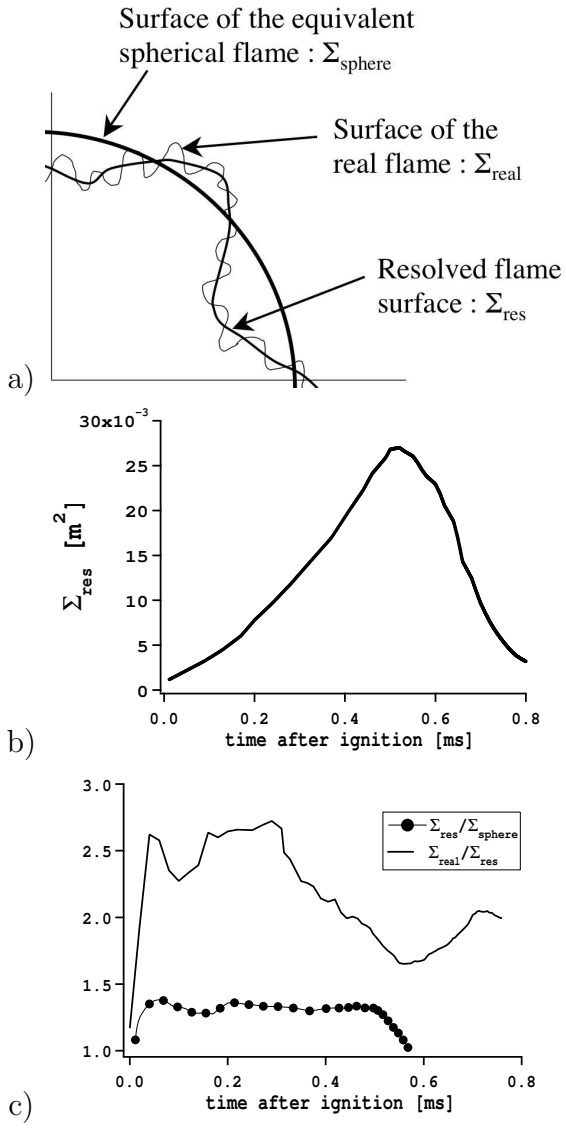

Fig. 27. Flame surface and wrinkling. a) Sketch of the different flame surfaces. b) Resolved flame surface Σ_{res} (based on the 1000K iso-surface). c) Comparison of the resolved wrinkling ($\frac{\Sigma_{res}}{\Sigma_{sphere}}$) and the sub-grid-scale wrinkling ($\frac{\Sigma_{real}}{\Sigma_{res}}$) averaged on the flame surface.